

# Quantum fluid dimers of hyperbolic exciton-polariton condensates

Ioannis Georgakilas,<sup>1,2,\*</sup> Antonio Gianfrate,<sup>3,\*</sup> Dimitrios Trypogeorgos,<sup>3,†</sup> Helgi Sigurðsson,<sup>4,5</sup> Fabrizio Riminucci,<sup>6</sup> Kirk W. Baldwin,<sup>7</sup> Loren N. Pfeiffer,<sup>7</sup> Milena De Giorgi,<sup>3</sup> Dario Ballarini,<sup>3</sup> and Daniele Sanvitto<sup>3</sup>

<sup>1</sup>*IBM Research–Zurich, Säumerstrasse 4, CH-8803 Rüschlikon, Switzerland*

<sup>2</sup>*Institute of Quantum Electronics, ETH Zurich, Auguste-Piccard-Hof 1, 8093 Zürich, Switzerland*

<sup>3</sup>*CNR Nanotec, Institute of Nanotechnology, via Monteroni, 73100, Lecce, Italy*

<sup>4</sup>*Institute of Experimental Physics, Faculty of Physics,*

*University of Warsaw, ul. Pasteura 5, PL-02-093 Warsaw, Poland*

<sup>5</sup>*Science Institute, University of Iceland, Dunhagi 3, IS-107 Reykjavik, Iceland*

<sup>6</sup>*Molecular Foundry, Lawrence Berkeley National Laboratory,*

*One Cyclotron Road, Berkeley, California, 94720, USA*

<sup>7</sup>*PRISM, Princeton Institute for the Science and Technology of Materials,*

*Princeton University, Princeton, New Jersey 08540, USA*

(Dated: December 19, 2024)

Coupled many-body quantum systems give rise to rich emergent physics and abundance of both stationary and dynamical behaviours. Designing platforms with tunable and distinct forms of coupling gives new insight into the collective behaviour of the dimerised quantum systems. Fundamentally, two systems can exchange particles through either forbidden or allowed channels, underpinning evanescent and ballistic coupling mechanisms, respectively. Based on proximity, the former leads to large spectral splitting that defines, for instance, chemical binding energies, whereas the latter pushes for stringent phase-matching and synchronicity between oscillating degrees-of-freedom, analogous to phase-coupled harmonic oscillators, with a significantly smaller impact on the energy landscape. Here, we demonstrate an all-optically tunable evanescent-ballistic quantum fluid dimer based on hyperbolic exciton-polariton condensates in a photonic crystal waveguide. By changing the angle of the polariton dimer relative to the grating, the system transitions from an evanescently-coupled molecule with large mode-splitting to a ballistic condensate dimer with strict phase-matching conditions and rich interference patterns. We directly measure the condensate spectral features and mass flow subject to a saddle dispersion relation, and connect our results to mean field theory. These results showcase the potential of photonic crystals to study condensed matter phenomena lying at the interface between delay-coupled nonlinear oscillators and tight binding physics.

From sub-atomic particles, to atoms, to molecules, our physical universe emerges from interacting elementary particles. For systems that approach a mesoscopic size the details of their shared wavefunction depend on the nature of their coupling. For the most part, a coupled phase-amplitude oscillator model is illustrative of the two possible mechanisms: quantum systems will either synchronise in phase or open spectral gaps and initiate dynamical oscillation when in proximity with each other. These two fundamentally different mechanisms are responsible, on the one hand, for various synchronisation [1] and ballistic transport [2] phenomena and, on the other hand for, the emergence of band structures in tight binding models [3], and super- and sub-radiance in arrays of quantum emitters [4, 5]. Continuously tuning between the nature of the coupling between these two regimes likely requires a quantum fluid with mixed periodic and continuous translation symmetry, a situation which can be engineered in artificial systems. Here, we demonstrate how this is possible in hyperbolic photonic crystal exciton-polaritons waveguides.

Exciton-polaritons (polaritons from hereon) are bosonic light-matter quasiparticles that form under the strong coupling of confined photons and quantum well excitons [6]. They possess a small effective mass and strong Coulomb interactions making their nonequilibrium condensation possible at elevated temperatures across a breadth of materials [7]. The coupling between neighbouring polariton condensates is defined by their engineered potential landscape, excitation technique, on-site energy, and separation distance which gives access to a variety

of distinct polariton Hamiltonians [8]. As such, considerable effort has been dedicated towards controlling the environment and potential landscape and, consequently, the coupling between polariton condensates through intricate sample fabrication and patterning [9] and all-optical techniques [10–14].

To date, mode hybridization and population oscillations of deeply confined evanescently-coupled polariton condensates have been confirmed between accidental sample defects [15] or in pre-designed photonic micropillar molecules [16, 17]. There, the usual tight-binding approach, supplemented with non-Hermitian terms, captures the essential physics between coupled polariton condensates. In contrast to deeply confined condensates, there are ballistic polariton condensates which are defined by strong radial polariton outflow and stringent phase matching conditions between neighbours that defines their synchronisation [10, 13, 18–20]. These ballistic condensates appear when pumped with a tightly focused beams which lead to spatially localised blueshift and gain and strong out-of-equilibrium polariton behaviour.

Here we propose a system of reduced symmetry, in contrast to cylindrically symmetric planar microcavities, to access a new geometric tuning parameter for the inter-condensate coupling mechanism. Our system is a subwavelength grating waveguiding slab with multiple embedded quantum wells [see schematic Fig. 1] that supports optically reconfigurable bound-in-the-continuum (BiC) polariton condensates [14, 21]. The properties of BiC polaritons are notably different from conventional cavity polariton platforms. They exhibit extremely

low radiative decay rates, which decrease their condensation threshold by orders of magnitude [21–23] as compared to ballistic condensates [19]. As such they can achieve high densities, and are ideally suited for the study of highly nonlinear quantum hydrodynamics [24–26] that requires long spatio-temporal coherence scales [27]. When dimerised, in this highly anisotropic photonic crystal, the angle of the axis connecting two condensates, with respect to the grating direction, plays a pivotal role in determining whether the coupling mechanism can be interpreted as evanescent or ballistic in origin, or a mixture of the two. The ability to continuously tune between the two natures of inter-condensate coupling introduces a new paradigm in polaritonic lattice systems, which until now have remained limited to either fully ballistic or fully evanescent coupling mechanisms.

### I. EVANESCENT AND BALLISTIC AXIS

The studied waveguide has a two-dimensional slab geometry, with the grating along one direction ( $y$ ) and quasicontinuous translation symmetry along the other ( $x$ ). Here, the lowest energy polariton branch forms a saddle dispersion centred at  $k = 0$  [see Fig. 1a] where  $\mathbf{k} = (k_x, k_y)^T$ ,

$$\hat{\epsilon}(\mathbf{k}) - \epsilon_0 = \frac{\hbar^2}{2} \left( \frac{k_x^2}{m_x} - \frac{k_y^2}{m_y} \right). \quad (1)$$

This dispersion relation is in sharp contrast to typical planar polariton cavities which are described by a paraboloids,  $\hat{\epsilon}(\mathbf{k})_{\text{par}} = \hbar^2 k^2 / 2m$  due to cylindrical symmetry. Here,  $\epsilon_0$  is the energy of the lower branch polaritons at normal incidence and  $m_{x,y}$  denote the magnitude of the effective masses along each direction. Along the grating direction,  $\hat{y}$ , lower energy antisymmetric polaritons obtain a large negative effective mass [see Fig. 1b] because guided photon modes fold across the Brillouin zone and open a gap at  $k_y = 0$  [28], whereas in the perpendicular direction,  $\hat{x}$ , they don't sense the grating and retain their positive effective mass [see Fig. 1c] from standard photon confinement along the  $z$ -direction. More details on the full polariton dispersion is shown in the Supplemental Information (SI).

The anisotropy of the saddle dispersion gives a marked directionality in the coupling mechanism between two neighbouring condensates, driven by two nonresonant pump spots (Gaussian beams) focused on the grating [see Fig. 1f],

$$P(\mathbf{r}) = e^{-|\mathbf{r}-\mathbf{r}_1|^2/2w^2} + e^{-|\mathbf{r}-\mathbf{r}_2|^2/2w^2}. \quad (2)$$

The separation distance between the two condensates is denoted by  $r = |\mathbf{r}_1 - \mathbf{r}_2|$  and the angle of their link with respect to the  $x$ -axis as  $\theta$ . The nonresonant pumps not only sustain the condensates above threshold, but also photoexcite an incoherent background of charge carriers and excitons which, due to the strong Coulomb interactions of excitons, results in large polariton blueshifts. In this sense, the pump profile is proportional to an effective potential landscape  $P(\mathbf{r}) \propto V(\mathbf{r}) > 0$  felt by the polaritons [14]. Because of the pump-induced potential gradient, positive and negative effective mass polaritons,

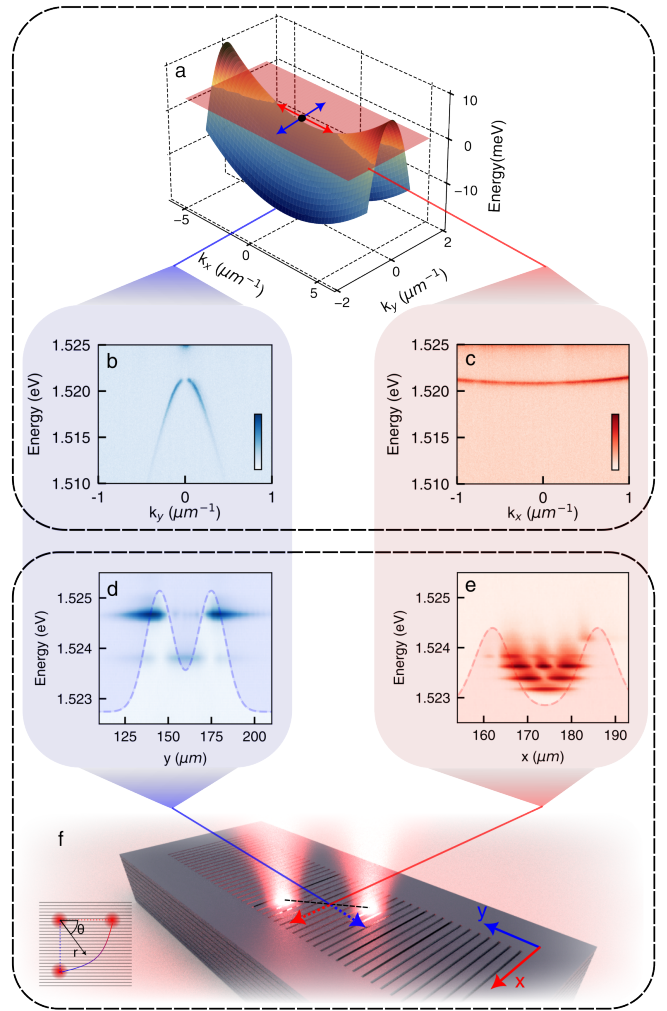


FIG. 1. **System and geometry.** **a.** 3D representation of the dispersion of the polaritonic waveguide. The lowest-energy mode, where condensation takes place, has a hyperbolic, saddle-like, dispersion which inverts the effective mass of the two principal reciprocal directions. **b** and **c.** Dispersions along  $k_x$  and  $k_y$  showing the different effective mass in the lower branch. **d** and **e.** The energy-resolved emission from a polariton dimer in coordinate space. Overlaid is the effective potential created by the pump spots that is attractive in **d** and repulsive in **e**. The potentials are drawn taking the effective mass into account, in such a way that the condensate forms in the non-coloured area. **f.** Schematic of the pump profiles on the grating waveguide. The coupling is ballistic (evanescent) along the  $x$ -axis ( $y$ -axis).

are 'repelled from' and 'attracted to' their pumped regions respectively [see Fig. 1de where the potentials have been drawn taking into account the difference in the effective mass].

Each scenario displays qualitatively different behaviour. Negative-mass polaritons experience the two pumps as a double potential well that traps them deeply [see Fig. 1d]. On the other hand, positive mass polaritons experience the two pumps as potential barriers, that trap instead particles between them [see Fig. 1e] [18, 29]. For this reason, the two directional

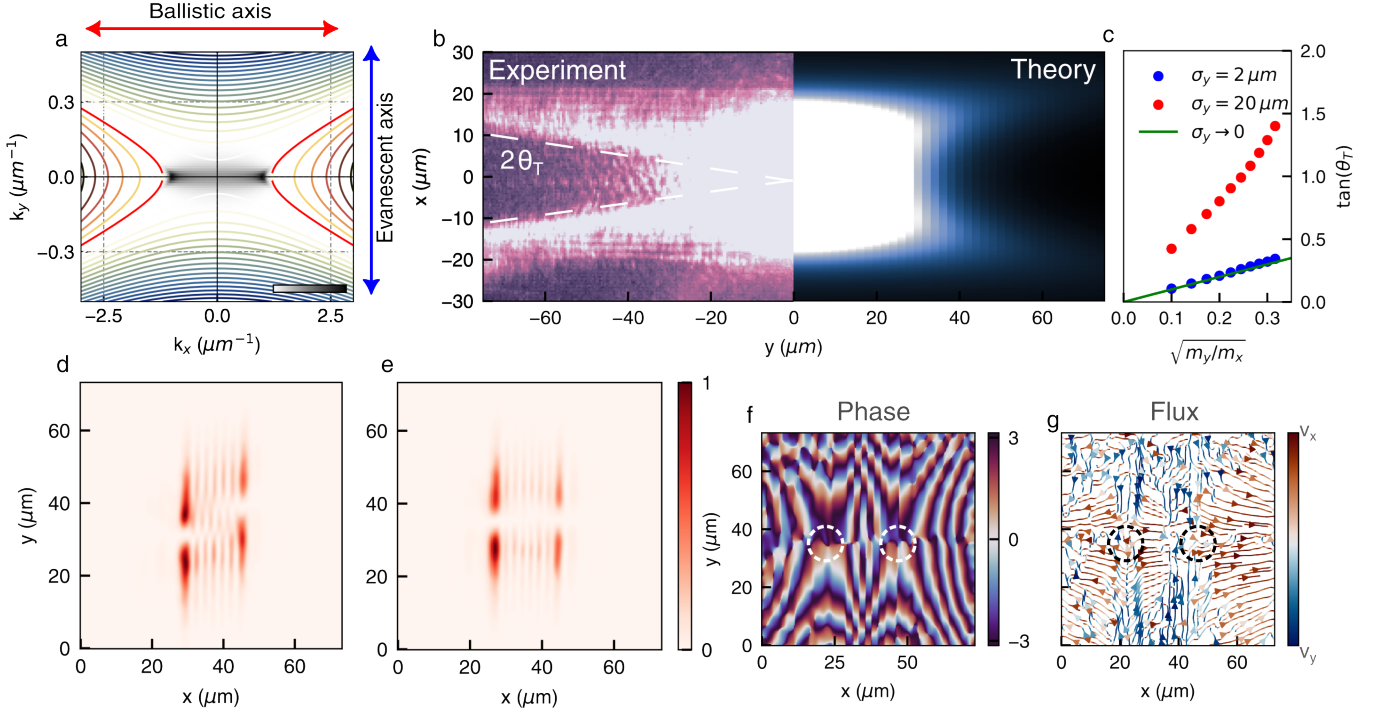


FIG. 2. **Polariton flow on hyperbolic contours.** **a.** Iso-energetic curves at a blueshift of 0.4 meV from the saddle point showing two opposite hyperbolas. Along  $k_x$  the dispersion is convex parabolic leading to strong polariton outflow and ballistic coupling (red arrow), while along  $k_y$  it is concave parabolic (negative effective mass) which leads to optical trapping and evanescent coupling (blue arrow) of the condensates. The calculated reciprocal-space PL for a single condensate on the saddle dispersion is superimposed. **b.** Oversaturated coordinate-space PL above condensation threshold. Since, along the  $y$  direction, there exist no available states for the polaritons to scatter to, propagation is not allowed within a cone of about  $\pm 10^\circ$ , left experiment, right theory. **c.** Dependence of  $\theta_T$  on the mass ratio and the size of the pump spot from simulations. **d-e.** Coordinate-space PL of two condensates at different angles in the ballistic regime. The fringes show high directionality and are always oriented along  $y$ . **f-g.** The overall flow is better visualised from the phase and velocity images showing inflow (outflow) of polaritons along the  $x$ -axis ( $y$ -axis). The red-blue colorscale of the velocity arrows denotes their directionality as  $|\arctan(v_x/v_y)|$ .

extremes  $\theta = 0^\circ$  and  $90^\circ$  are referred to as the *ballistic* and *evanescent* coupling directions, respectively, corresponding to the dominant coupling mechanism. Along the evanescent  $y$ -direction, slowly varying condensed polaritons tunnel through a forbidden region resulting in mode hybridization with a consequent bonding and an antibonding level Fig. 1d separated by  $\sim$ meVs in energy [14]. Orienting the two pump spots along the ballistic  $x$ -direction, however, condensed polaritons couple to propagating modes between the pump spots resulting in a so-called ballistic coupling mechanism. Here, the two pump spots form a double-barrier potential along the ballistic  $x$ -axis with propagating positive-mass polaritons forming many standing wave resonances whose smaller energy spacing [see Fig. 1e] is given by the distance between pump spots, similar to results reported for in planar cavities [19].

The observed directional evanescent and ballistic coupling mechanisms can be appreciated from the opposite-facing isofrequency hyperbolas in the polariton saddle dispersion relation [see Fig. 2a],

$$k_y = \pm \sqrt{m_y \left( \frac{k_x^2}{m_x} - \frac{2\epsilon_c}{\hbar^2} \right)}. \quad (3)$$

The aspect ratio of these hyperbolas is determined by the effective mass ratio  $m_x/m_y$  that, in our system, is  $\approx 100$  by comparing Fig. 1b and Fig. 1c. Here, we have set  $\epsilon_0 = 0$  without loss of generality, and  $\epsilon_c > 0$  is the energy of the condensate which is set by the laser power (pump-induced blueshift). Condensed polaritons populate a pair of opposite-facing hyperbolic contours in the dispersion, which results in strong anisotropic PL (density) distribution for the single condensate shown in Fig. 2b with an oversaturated colorscale. Along the evanescent  $y$ -direction the polaritons find no available states to scatter to, whereas along the ballistic  $x$ -direction their outward flow is possible but with a much heavier mass. This yields a polariton “propagation cone” separating a dark forbidden region from a brighter ballistic region. The angle of the real-space cone  $\theta_T$  is reciprocally related to the slopes of the populated hyperbolic contours, which, in the asymptotic limit  $k \rightarrow \infty$  is  $s = \pm \sqrt{m_y/m_x}$ . Therefore, for a small pump spot that excites large-wavenumber polaritons, we obtain  $\theta_T \rightarrow \arctan(\sqrt{m_y/m_x}) = 5.7^\circ$ , which is in reasonable agreement with the experimental extent of the forbidden region  $\approx 10^\circ$ . The small mismatch is due to the finite size of the trap. The simulated  $\theta_T$  for  $\sigma_y = 2 \mu\text{m}$  and  $20 \mu\text{m}$  is shown in Fig. 2c. The corresponding calculated reciprocal space

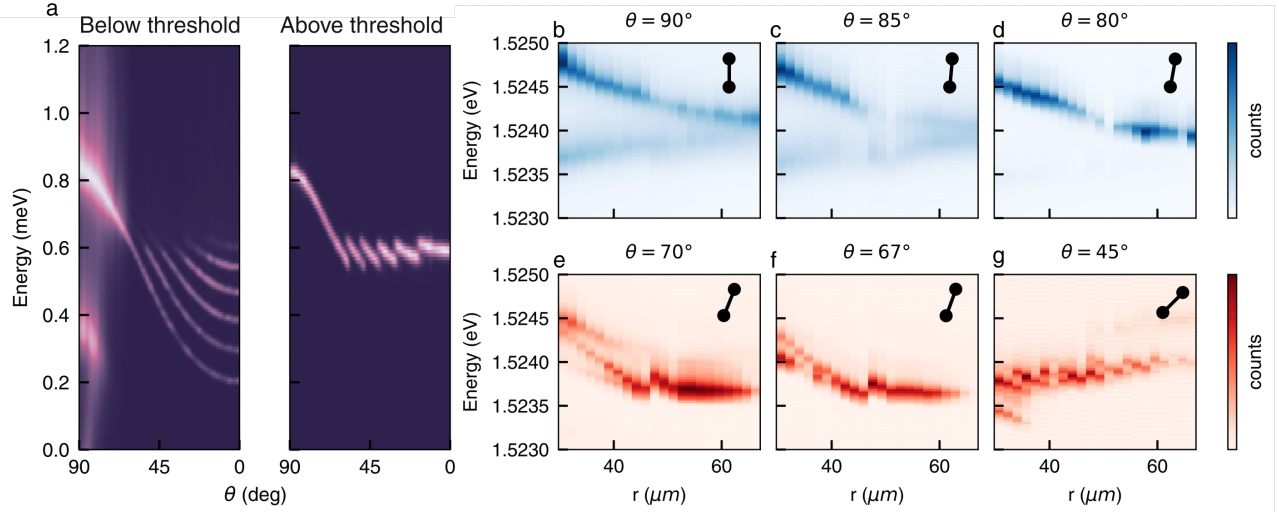


FIG. 3. **Transition between evanescent and ballistic coupling regimes.** **a** Calculated spectrum of the polariton dimer over angle for a fixed distance of  $30 \mu\text{m}$ , below condensation threshold left, above right. **b-g** PL showing the energy spectrum over distance  $r$ , for various angles  $\theta$ . The energy gap of the dimer decreases by increasing distance. When entering the ballistic regime **e-g** we observe the characteristic mode-flipping between the in-phase and anti-phase configurations. The energy for  $r \ll 1$  asymptotically goes to that of a single condensate; slight variations of the order of  $300 \mu\text{eV}$  are due to 5% fluctuations in the laser power.

condensate density for  $\sigma_y = 20 \mu\text{m}$  is shown in Fig. 2a overlapped with the dispersion contours. Notice the two maxima at  $k_c \approx \pm 1 \mu\text{m}^{-1}$  which define the wavenumber of ballistic polariton waves along the  $x$ -direction.

Figures 2d-e show example coordinate space PL distributions of the condensate dimer for two different angles  $\theta = 26^\circ$  and  $0^\circ$ . We note that the central nodal line in each condensate is a property of the BiC state [21]. Between the condensates multiple interference fringes appear due to positive-mass propagating waves reflecting back-and-forth between the pump spots. As the projection of the dimer link on the ballistic  $x$ -axis reduces with larger angle,  $r_x = r \cos(\theta)$ , the number of interference fringes between the spots also reduces. This can be seen in Fig. 2d where the number of fringes are 5 whereas in Fig. 2e they are 6. Namely,  $r_x$  is reduced by  $\lambda_c/2$ , where  $\lambda_c = \sqrt{2\pi^2 \hbar^2 / m_x \epsilon_c}$  is the average wavelength of the ballistic component of the condensates. Analogously, the condensates can be said to have undergone a transition from an anti-phase synchronous (even number of fringes) to an in-phase synchronous (odd number of fringes) state. As the dimer angle  $\theta$  is increased further, the condensate dimer passes through more synchrony transitions until it enters the evanescent regime [14].

Figures 2f and 2g show the extracted condensate dimer phase and velocity maps corresponding to Fig. 2e. Positive-mass polaritons obtain an outward velocity component along the  $x$ -direction with respect to their pump spots, whereas along the  $y$ -axis negative-mass polaritons acquire an inward velocity component and are attracted to their pump spots.

## II. HYBRID DIRECTIONAL COUPLING

The angular and radial dependence of the coupling mechanism between the two condensates can be described by a simple coupling parameter coming from their overlap integral. Using an appropriate ansatz composed of propagating and evanescent waves along each direction [see SI] we obtain the following,

$$J(r, \theta) \propto \int \psi(\mathbf{r}_1)^* \psi(\mathbf{r}_2) d\mathbf{r}, \quad (4)$$

$$= \cos(k_c r_x) e^{-\kappa r_x} e^{-(r^2 - r_x^2)/8\sigma_y^2}.$$

Here,  $k_c = 2\pi/\lambda_c$  is the average wavenumber of the condensate outgoing waves,  $\kappa \sim \gamma m_x / 2\hbar k_c$  is a damping coefficient due to the polariton lifetime  $\gamma^{-1}$ , and  $\sigma_y$  defines the size of the trapped condensate along the  $y$ -direction. The number of interference fringes between the condensates is associated with the  $n$ th root of the cosine function [18]. For  $J > 0$  the condensates synchronise in-phase whereas for  $J < 0$  they synchronise anti-phase in order to maximise the gain and amplitude of the dimer. Here we focus on the optically tunable transition between the two coupling regimes. Figure 3a shows the calculated polariton spectral density for two pump spots as a function of  $\theta$ , below and above condensation threshold. For a dimer orientated along the evanescent axis,  $\theta = 90^\circ$ , the spectrum reveals the bonding (upper) and antibonding (lower) branches [14]. The reason the bonding branch is higher in energy, as opposed to being lower like in atomic orbital theory, is because energy-level hierarchy inverts when the effective mass is negative. As  $\theta$  is decreased, the two major branches red-shift revealing the appearance of additional branches, above  $> 45^\circ$ , corresponding to the resonances of the ballistic polari-

ton dimer [18, 19, 29]. Above threshold, the sharp spectral density of the condensate appears to jump from one resonance branch to the next when sweeping  $\theta$ , signifying transitions from in-phase to anti-phase synchronization, and so on [18, 19].

Corresponding experimental images are shown in Fig. 3b-g as a function of separation distance  $r$  and angle  $\theta$ , between  $90^\circ$  to  $45^\circ$  since for  $\theta < 45^\circ$  the system is well into the ballistic regime and its spectral signature does not change significantly. In the evanescent regime, the splitting between the bonded and the antibonded branches decreases as  $e^{-r^2}$ , as shown in Fig. 3b-d, with polaritons becoming largely non-interacting at distances larger than  $r > 100 \mu\text{m}$ . For small separations of  $r < 30 \mu\text{m}$ , so that the two optical traps do not overlap significantly, we measured a considerable spectral gap of 1.1 meV at  $\theta = 90^\circ$  which is one order of magnitude larger than the polariton linewidth of  $100 \mu\text{eV}$ . The trap overlap sets the maximum spectral gap attainable which decreases as  $e^{-\sin^2 \theta}$  going towards the ballistic regime. This spatial dependence of  $J$  can be seen clearly in Fig. 4a.

As  $\theta$  decreases, going from the evanescent to the ballistic regime, shown in Fig. 3e-g, the bonding branch shows a gradual redshift while at the same time the antibonding branch gradually disappears, in agreement with theory shown Fig. 3a. Close to  $70^\circ$ , Fig. 3e-f, the spectra starts showing characteristics of both coupling types; a considerable blueshift for distances lower than  $40 \mu\text{m}$ , due to the condensate wavefunction overlap along the evanescent axis, together with the appearance of a substructure with an energy splitting in the order of  $100 \mu\text{eV}$  when in the ballistic coupling regime. Similar features can be identified in coordinate space, by looking at the characteristic magnitude of the energy splitting between distinct modes and the number of interference fringes between the condensates in their spatial PL profile [see Fig. 1e].

Figure 4b shows the number of fringes ranging from 2 to 10. The increasing number of fringes with the spatial separation at small angles is similar to ballistic coupled condensates in microcavities [19]. A new fringe enters the inter-condensate region every time the distance increases by more than an integer multiple of the fringe separation  $\lambda_c/2$ . Differently from planar microcavities however, for a hyperbolic dispersion the outward ballistic polariton flow from each condensate is bounded by an in-plane “propagation-cone”, forming a polariton jet of propagating waves with well-defined in-plane momenta [see Fig. 2b]. If the two condensates are within each-other’s cone aperture, ballistic coupling ensues. Figure 4c, shows the observed number of fringes as a function of either the radial distance  $r$  or projected distance  $r_x$ . While the number of fringes is weakly dependent on  $r$ , the data distribution shows a clear linear trend as a function of  $r_x$  with a slope  $k_c r_x / \pi$  according to Eq. (4), corresponding to phase accumulation of propagating ballistic waves. The extracted wavelength of outflowing condensate waves is  $2\pi/k_c = \lambda_c \approx 6.6 \mu\text{m}$  which is in good agreement with the two maxima in the calculated momentum space PL in Fig. 2a (black intensity maxima).

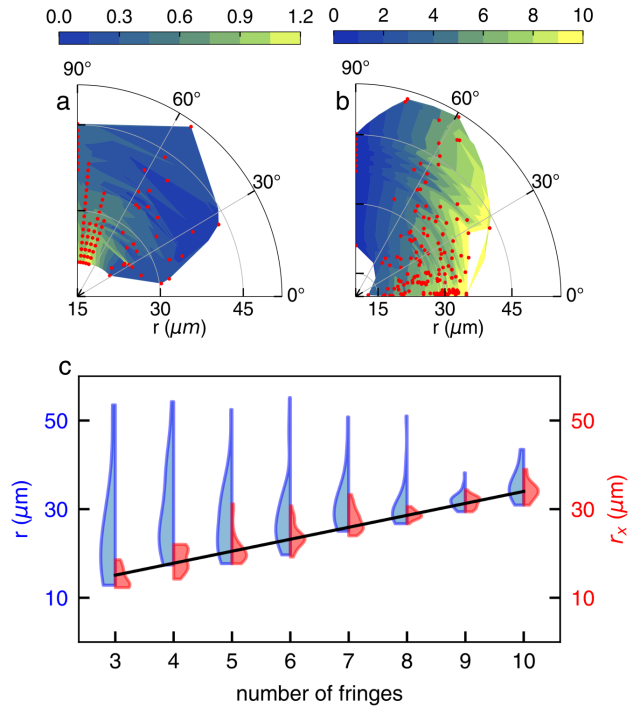


FIG. 4. **Directional coupling.** Energy splitting **a** and number of interference fringes **b** in the condensate dimer as a function of angle  $\theta$  and distance  $r$ . The evanescent coupling decreases monotonically with both  $\theta$  and  $r$ , ranging from 1.4 meV to 0.1 meV. The ballistic coupling changes for in- to anti-phase with  $r_x$ , however it remains largely constant as long as  $\theta < 45^\circ$ . The red points indicate the coordinates of the measurements we used to extract the two couplings. The two colorbars indicate the width of the energy gap **a** and the number of fringes **b**. **c**. Statistical averages of the number of fringes for increasing distance between the condensates plotted as a function of  $r$  and  $r_x$ . The width of the distribution is significantly smaller for  $r_x$  showcasing the directionality of the system. The black line denotes the linear phase accumulation  $k_c r_x / \pi$  of waves propagating between the condensates.

### III. DISCUSSION AND CONCLUSIONS

We have engineered a polaritonic platform based on a photonic crystal waveguide that exhibits the simultaneous presence of both evanescent and ballistic couplings and can smoothly transition between the two. The nature of the coupling can be fully controlled geometrically by varying the angle connecting the polariton dimers. These unique spatial features originate from the underlying hyperbolic dispersion of the system that we measured using reciprocal-space imaging. A parabolic dispersion along  $k_x$  and a negative effective mass along  $k_y$  lead to the ballistic and evanescent coupling of polaritons respectively. We provided a corresponding picture of the physics of BiC polariton condensates in coordinate space in terms of localisation geometry and in-plane fluxes. We showed that within a coordinate space circular sector, ballistic propagation is forbidden. Conversely, along the transverse direction, polariton propagation is characterised by a unidirectional flow

with well-defined momenta. At the critical angle where the propagation cone appears the coupling transitions between the two variants cross a region where both types of couplings coexist.

We demonstrated reconfigurable formation of polariton dimers for a variety of distances and angles, fully mapping the positive quadrant. The knowledge of the spatial dependence of the coupling is crucial for designing of complex networks of polaritons. Driven-dissipative networks of exciton-polariton Bose-Einstein condensates form a promising nonlinear optical platform for simulation of artificial lattices [8, 12, 30] and spin Hamiltonians [11, 31], studying universal scaling laws [27], topological physics [32], and implementing neural-inspired optical computation protocols [33]. Our system goes beyond what is currently possible in the implementation of such networks given that the nature of the coupling parameter displays a highly anisotropic dependence on angle. As such, our dimers constitute an integral building component of advanced analogue polaritons simulators.

Insofar, we have ignored the non-trivial BiC topology, however it adds an additional powerful tool for engineering the coupling of system without depending exclusively on the changing effective mass. The topology in coordinate space manifests as a  $\pi$  phase difference between the two lobes which can lead to interesting phase structures depending on the position of the pumping sites. The highly directional flow of polaritons that ensues between two pumping spots at a finite angle leads to their phase locking and at the same time develops a linear phase dislocation in the inter-condensate region; a single lobe of any given phase cannot satisfy the phase constraints when interacting with both lobes of another BiC that have a  $\pi$  phase jump. This attests to how topology can be used to enrich the physics of the coupled dimers even further. Reducing the underlying symmetry of the system from  $C_2$  to  $C_4$ , by imprinting a two-dimensional grating, effectively gives the same behaviour but at half-angle which can lead to tighter arrangement of pumping sites and more compact systems; however, note that the fundamental mechanism is perfectly contained in our one-dimensional waveguide. Our platform provides a foundation for other studies to build upon and suggests novel paths of investigation using high-field trapped polaritons in a tight-binding setting.

**Acknowledgements.** We acknowledge fruitful discussions with R. Mahr and T. Stöferle. This project was funded by PNRR MUR project: ‘National Quantum Science and Technology Institute’ - NQSTI (PE0000023); PNRR MUR project: ‘Integrated Infrastructure Initiative in Photonic and Quan-

tum Sciences’ - I-PHOQS (IR0000016); EU H2020 MSCA-ITN project ‘AppQInfo’ (Grant Agreement No. 956071); Quantum Optical Networks based on Exciton-polaritons - (Q-ONE) funding from the HORIZON-EIC-2022-PATHFINDER CHALLENGES EU programme under grant agreement No. 101115575; Neuromorphic Polariton Accelerator - (PolArt) funding from the Horizon-EIC-2023-Pathfinder Open EU programme under grant agreement No. 101130304; the project ‘Hardware implementation of a polariton neural network for neuromorphic computing’ – Joint Bilateral Agreement CNR-RFBR (Russian Foundation for Basic Research) – Triennial Program 2021–2023; the MAECI project ‘Novel photonic platform for neuromorphic computing’, Joint Bilateral Project Italia - Polonia 2022-2023; the PRIN project ‘QNoRM: A quantum neuromorphic recognition machine of quantum states’ - (grant 20229J8Z4P). Views and opinions expressed are however those of the author(s) only and do not necessarily reflect those of the European Union or European Innovation Council and SMEs Executive Agency (EISMEA). Neither the European Union nor the granting authority can be held responsible for them. This research is funded in part by the Gordon and Betty Moore Foundation’s EPiQS Initiative, grant GBMF9615 to L.P., and by the National Science Foundation MRSEC grant DMR 2011750 at Princeton University. Work at the Molecular Foundry is supported by the Office of Science, Office of Basic Energy Sciences, of the U.S. Department of Energy under Contract No. DE-AC02-05CH11231. We thank Scott Dhuey for assistance with electron beam lithography and Paolo Cazzato for the technical support. H.S. acknowledges the Icelandic Research Fund (Rannís), grant No. 239552-051, and the project No. 2022/45/P/ST3/00467 co-funded by the Polish National Science Centre and the European Union Framework Programme for Research and Innovation Horizon 2020 under the Marie Skłodowska-Curie grant agreement No. 945339.

**Competing interests.** The authors declare no competing interests.

**Data Availability.** The data of this study is available from the corresponding author upon reasonable request.

**Author contributions.** IG and AG took the data and together with DT performed the analysis. AG, HS and DT wrote the manuscript. HS led the theory. FR processed the sample; growth was performed by KB and LP. DS supervised the work and discussed the data. All authors contributed to discussions and editing of the manuscript.

\* These two authors contributed equally.

† [dimitrios.trypogeorgos@nanotec.cnr.it](mailto:dimitrios.trypogeorgos@nanotec.cnr.it)

- [1] J. A. Acebrón, L. L. Bonilla, C. J. Pérez Vicente, F. Ritort, and R. Spigler, *Rev. Mod. Phys.* **77**, 137 (2005).  
 [2] V. E. Calado, S. Goswami, G. Nanda, M. Diez, A. R. Akhmerov, K. Watanabe, T. Taniguchi, T. M. Klapwijk, and L. M. K. Vandersypen, *Nature Nanotechnology* **10**, 761 (2015).  
 [3] N. W. Ashcroft and N. D. Mermin, *Solid State Physics* (Harcourt

College Publishers, New York; London, 1976).

- [4] S. J. Masson and A. Asenjo-Garcia, *Nature Communications* **13**, 2285 (2022).  
 [5] H. Yu, G.-B. Liu, J. Tang, X. Xu, and W. Yao, *Science Advances* **3**, e1701696 (2017).  
 [6] H. Deng, H. Haug, and Y. Yamamoto, *Rev. Mod. Phys.* **82**, 1489 (2010).  
 [7] S. Ghosh, R. Su, J. Zhao, A. Fieramosca, J. Wu, T. Li, Q. Zhang,

- F. Li, Z. Chen, T. Liew, D. Sanvitto, and Q. Xiong, *Photonics Insights* **1**, R04 (2022).
- [8] A. Amo and J. Bloch, *Comptes Rendus Physique* **17**, 934 (2016), polariton physics / Physique des polaritons.
- [9] C. Schneider, K. Winkler, M. D. Fraser, M. Kamp, Y. Yamamoto, E. A. Ostrovskaya, and S. Höfling, *Reports on Progress in Physics* **80**, 016503 (2016).
- [10] S. Alyatkin, J. D. Töpfer, A. Askitopoulos, H. Sigurdsson, and P. G. Lagoudakis, *Phys. Rev. Lett.* **124**, 207402 (2020).
- [11] R. Tao, K. Peng, L. Haeberlé, Q. Li, D. Jin, G. R. Fleming, S. Kéna-Cohen, X. Zhang, and W. Bao, *Nature Materials* **21**, 761 (2022).
- [12] H. Ohadi, A. J. Ramsay, H. Sigurdsson, Y. del Valle-Inclan Redondo, S. I. Tsintzos, Z. Hatzopoulos, T. C. H. Liew, I. A. Shelykh, Y. G. Rubo, P. G. Savvidis, and J. J. Baumberg, *Phys. Rev. Lett.* **119**, 067401 (2017).
- [13] D. Dovzhenko, D. Aristov, L. Pickup, H. Sigurdsson, and P. Lagoudakis, *Phys. Rev. B* **108**, L161301 (2023).
- [14] A. Gianfrate, H. Sigurdsson, V. Ardizzone, H. C. Nguyen, F. Riminucci, M. Efthymiou-Tsironi, K. W. Baldwin, L. N. Pfeiffer, D. Trypogeorgos, M. De Giorgi, D. Ballarini, H. S. Nguyen, and D. Sanvitto, *Nature Physics* **20**, 61 (2024).
- [15] K. G. Lagoudakis, B. Pietka, M. Wouters, R. André, and B. Deveaud-Plédran, *Phys. Rev. Lett.* **105**, 120403 (2010).
- [16] M. Galbiati, L. Ferrier, D. D. Solnyshkov, D. Tanese, E. Wertz, A. Amo, M. Abbarchi, P. Senellart, I. Sagnes, A. Lemaître, E. Galopin, G. Malpuech, and J. Bloch, *Phys. Rev. Lett.* **108**, 126403 (2012).
- [17] M. Abbarchi, A. Amo, V. G. Sala, D. D. Solnyshkov, H. Flayac, L. Ferrier, I. Sagnes, E. Galopin, A. Lemaître, G. Malpuech, and J. Bloch, *Nature Physics* **9**, 275 (2013).
- [18] H. Ohadi, R. L. Gregory, T. Freearde, Y. G. Rubo, A. V. Kavokin, N. G. Berloff, and P. G. Lagoudakis, *Phys. Rev. X* **6**, 031032 (2016).
- [19] J. D. Töpfer, H. Sigurdsson, L. Pickup, and P. G. Lagoudakis, *Communications Physics* **3**, 2 (2020).
- [20] M. Furman, R. Mirek, M. Król, W. Pacuski, H. Sigurdsson, J. Szczytko, and B. Piętka, *Communications Physics* **6**, 196 (2023).
- [21] V. Ardizzone, F. Riminucci, S. Zanotti, A. Gianfrate, M. Efthymiou-Tsironi, D. G. Suárez-Forero, F. Todisco, M. De Giorgi, D. Trypogeorgos, G. Gigli, K. Baldwin, L. Pfeiffer, D. Ballarini, H. S. Nguyen, D. Gerace, and D. Sanvitto, *Nature* **605**, 447 (2022).
- [22] F. Riminucci, A. Gianfrate, D. Nigro, V. Ardizzone, S. Dhuey, L. Francaviglia, K. Baldwin, L. N. Pfeiffer, D. Ballarini, D. Trypogeorgos, A. Schwartzberg, D. Gerace, and D. Sanvitto, *Physical Review Letters* **131**, 246901 (2023).
- [23] X. Wu, S. Zhang, J. Song, X. Deng, W. Du, X. Zeng, Y. Zhang, Z. Zhang, Y. Chen, Y. Wang, C. Jiang, Y. Zhong, B. Wu, Z. Zhu, Y. Liang, Q. Zhang, Q. Xiong, and X. Liu, *Nature Communications* **15**, 3345 (2024).
- [24] L. A. Smirnov, D. A. Smirnova, E. A. Ostrovskaya, and Y. S. Kivshar, *Phys. Rev. B* **89**, 235310 (2014).
- [25] G. Grosso, G. Nardin, F. Morier-Genoud, Y. Léger, and B. Deveaud-Plédran, *Phys. Rev. Lett.* **107**, 245301 (2011).
- [26] D. Trypogeorgos, A. Gianfrate, M. Landini, D. Nigro, D. Gerace, I. Carusotto, F. Riminucci, K. W. Baldwin, L. N. Pfeiffer, G. I. Martone, M. D. Giorgi, D. Ballarini, and D. Sanvitto, *Emerging supersolidity from a polariton condensate in a photonic crystal waveguide* (2024), arXiv:2407.02373 [cond-mat.mes-hall].
- [27] Q. Fontaine, D. Squizzato, F. Baboux, I. Amelio, A. Lemaître, M. Morassi, I. Sagnes, L. Le Gratiet, A. Harouri, M. Wouters, I. Carusotto, A. Amo, M. Richard, A. Minguzzi, L. Canet, S. Ravets, and J. Bloch, *Nature* **608**, 687 (2022).
- [28] H. Sigurdsson, H. C. Nguyen, and H. S. Nguyen, *Nanophotonics* **13**, 3503 (2024).
- [29] G. Tosi, G. Christmann, N. G. Berloff, P. Tsotsis, T. Gao, Z. Hatzopoulos, P. G. Savvidis, and J. J. Baumberg, *Nature Physics* **8**, 190 (2012).
- [30] S. Alyatkin, H. Sigurdsson, A. Askitopoulos, J. D. Töpfer, and P. G. Lagoudakis, *Nature Communications* **12**, 5571 (2021).
- [31] N. G. Berloff, M. Silva, K. Kalinin, A. Askitopoulos, J. D. Töpfer, P. Cilibrizzi, W. Langbein, and P. G. Lagoudakis, *Nature Materials* **16**, 1120 (2017).
- [32] D. D. Solnyshkov, G. Malpuech, P. St-Jean, S. Ravets, J. Bloch, and A. Amo, *Opt. Mater. Express* **11**, 1119 (2021).
- [33] A. Opala and M. Matuszewski, *Opt. Mater. Express* **13**, 2674 (2023).

## Supplementary Information

### I. SAMPLE AND EXPERIMENTAL METHODS

Our system is a 500 nm thick AlGaAs slab waveguide with 12 embedded 20 nm GaAs quantum wells. The surface of the slab hetero-structure is etched with a 170 nm deep grating and a 243 nm period with the purpose of optimizing the exciton-photon detuning (slightly negative) and the diffractive coupling between counterpropagating waveguided modes [see Fig. 1a]. The fabrication procedure is much simpler when compared to standard distributed Bragg reflector planar cavities, and is described in more detail in [1–3]. The exciton-photon detuning is roughly  $\Delta = -2.7$  meV, with a Rabi coupling strength of  $\Omega = 5.3$  meV. During the experiments the sample was held in a closed-loop helium cryostat at a temperature of 18 K. Polariton condensates were excited using off-resonant continuous-wave excitation beam with wavelength of 785 nm modulated at 350 Hz with an optical chopper with 10% duty cycle. A spatial light modulator was used to structure the beam into two Gaussian pump spots, each of size 3  $\mu\text{m}$  FWHM, the resulting luminescence i.e. the trap size is approximately 20  $\mu\text{m}$  FWHM. The spot size was mainly limited by the numerical aperture of the excitation objective.

### II. HYPERBOLIC DISPERSION OF THE LOWER POLARITON

The exciton-polariton dispersion of the photonic slab grating can be well approximated from diagonalizing a coupled oscillator model describing guided photon waves that coupling to excitons perpendicular ( $x$ ) and along ( $y$ ) to the grating direction. Here, we focus only on the TE mode which is closest to the exciton line and divide the photons into *forward* ( $\phi_{+1}$ ) and *backward* ( $\phi_{-1}$ ) propagating modes along the grating,

$$\hat{H}(\mathbf{k}) = \begin{pmatrix} \omega_X - i\gamma_X & \Omega & 0 & 0 \\ \Omega & \phi_{+1}(\mathbf{k}) & U - i\gamma & 0 \\ 0 & U - i\gamma & \phi_{-1}(\mathbf{k}) & \Omega \\ 0 & 0 & \Omega & \omega_X - i\gamma_X \end{pmatrix} \quad (\text{S1})$$

In the absence of the grating the guided photon modes are plane waves. In the presence of the grating opposite guided modes fold across the  $\Gamma$ -point in the  $k_y$  direction and couple to each other and lossy Fabry-Pérot modes inside the light cone [4]. The photon dispersion along the grating becomes approximately linear for low momenta whereas perpendicular to the grating it is quadratic with a positive effective mass [1],

$$\phi_{\pm 1} = -i\gamma \pm vk_y + \frac{\hbar^2 k_x^2}{2m}, \quad (\text{S2})$$

where  $\mathbf{k} = (k_x, k_y)^T$ . The group velocity of the photon along the  $x$ -direction is denoted  $v$ , and  $m$  is its effective mass along the  $y$ -direction. The light-matter coupling strength, also known as the *Rabi energy*, is denoted  $\Omega$  and the diffractive coupling between counterpropagating photon modes is  $U$ . The photon loss exchange mechanism with the radiative continuum is denoted with the parameter  $\gamma$ . Exciton losses are denoted as  $\gamma_X$ . Fitting the above Hamiltonian to the photoluminescence spectra from experiment we acquire the following set of parameters:

$\Omega$		5.3 meV
$U$		3.2 meV
$v$		36.2 meV $\mu\text{m}$
$\omega_X$		2.74 meV
$m$		0.28 meV ps <sup>2</sup> $\mu\text{m}^{-2}$

TABLE I. Parameters of the polariton dispersion obtained by fitting to experimental data.

The results of the study do not depend strongly on the values of decay rates. We have chosen  $\gamma = \gamma_X = 0.1U$  similar to previous studies [1]. The resulting full polariton dispersion is shown in Fig. S1. In the case of no exciton losses,  $\gamma_X = 0$ , the polariton losses for the *antisymmetric* polariton states above and below the exciton energy would be zero at the  $\Gamma$ -point, corresponding to the symmetry protected BiC. However, the presence of exciton losses  $\gamma_X \neq 0$  makes both BiCs in reality quasi-BiCs with finite lifetime [1]. Nevertheless, because of the negative detuning between the photon midgap energy and the exciton line the  $\Gamma$ -point in the lowest energy polariton branch possesses the lowest losses overall.



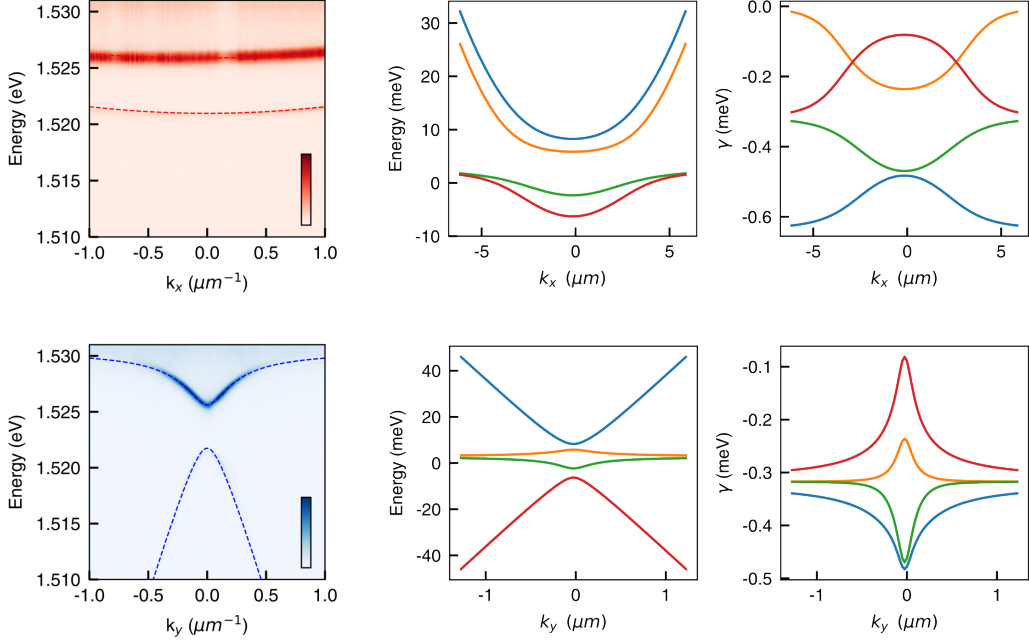


FIG. S1. Energy-momentum dispersion of polaritons in the photonic crystal waveguide along  $k_x$  (top row) and  $k_y$  (bottom row). The first column show the experimental dispersions. The dashed lines represent the eigenvalues of the Hamiltonian Eq. (S1). The data is obtained below condensation threshold which results in dominant PL coming from the upper bottleneck branches. The middle and last columns show all the eigenstates, including above the exciton energy, and the corresponding linewidths.

### III. SCALAR MEAN-FIELD APPROXIMATION

Due to interactions (thermalization) the lowest energy polariton branch is dominantly populated by the condensate, also stabilized by the BiC state, and we can disregard higher energy branches. For small momenta, the real part of the lowest energy polariton branch has a saddle-like structure with negative mass polaritons along the  $x$ -axis and heavier positive mass polaritons along the  $y$ -axis,

$$\hat{\epsilon}(\mathbf{k}) = \frac{\hbar^2}{2} \left( \frac{k_x^2}{m_x} - \frac{k_y^2}{m_y} \right). \quad (\text{S3})$$

Here,  $m_{x,y}$  can be estimated through polynomial fitting of the saddle surface coming from the lowest energy surface belonging to the eigenvalues of (S1). For the parameters in Table I, we obtain  $m_y/m_x \approx 101.8$ . The isofrequency curves (contours) of the saddle dispersion form opposite facing hyperbolas, e.g.,

$$k_y = \pm \sqrt{m_y \left( \frac{k_x^2}{m_x} - \frac{2E}{\hbar^2} \right)}. \quad (\text{S4})$$

Since the optically trapped BiC condensate is typically localized around small momenta in the photonic grating around and above threshold [1–3] we can make a scalar approximation and assign a wavefunction order parameter  $\psi(\mathbf{r}, t)$  describing the condensate in the near field for the lowest energy-branch polaritons, coupled to a nonresonantly driven reservoir of excitons  $n_R(\mathbf{r}, t)$  [4],

$$\begin{aligned} i \frac{\partial \psi}{\partial t} &= \left[ \hat{\epsilon}(-i\nabla) + g|\psi|^2 + g_R(n_R + \eta P(\mathbf{r})) + i \frac{R n_R}{2} \right] \psi, \\ \frac{\partial n_R}{\partial t} &= P(\mathbf{r}) - (\Gamma_R + R|\psi|^2)n_R. \end{aligned} \quad (\text{S5})$$

The first term contains the dispersion of the lowest energy polariton branch (including losses). The second term describes the short-range repulsive interaction between polaritons. Moreover, polaritons also interact repulsively with strength  $g_R > g$  against any background excitons whose density can be divided in to the bottleneck part  $n_R$  and a static inactive *dark* exciton background

parametrized by the dimensionless number  $\eta$ . The last term describes the stimulated scattering of reservoir excitons into the condensate at a rate  $R$ . The term  $P(\mathbf{r})$  describes the continuous-wave nonresonant pump which, for the condensate dimer, is a superposition of two spatially separated Gaussians,

$$P(\mathbf{r}) = P_0 \left( e^{-|\mathbf{r}-\mathbf{r}_1|^2/2w^2} + e^{-|\mathbf{r}-\mathbf{r}_2|^2/2w^2} \right). \quad (\text{S6})$$

Lastly,  $\Gamma_R$  is the average reservoir exciton decay rate. The parameters of the simulation are:  $g_R = 4g$ ,  $R = 10g$ ,  $\eta\Gamma_R = 6$ , and  $\Gamma_R = 0.2 \text{ ps}^{-1}$ .

#### IV. SPECTRAL DENSITY CALCULATIONS

Here, we show supplementary data from mean-field modelling Eq. (S5) supporting the experimental observations in Fig. 3 in the main text. The calculated spectral densities shown in Fig. 3a in the main text and Fig. S2 in the SM are obtained by averaging over the dynamics of Eq. (S5) over multiple independent random white-noise initial conditions (i.e., Monte-Carlo sampling). The calculations shown in Fig. S2 are performed below threshold ( $R$  is chosen to be sufficiently small) in order to avoid a narrow spectral peak belonging to the condensate dominating the rest of the spectral density.

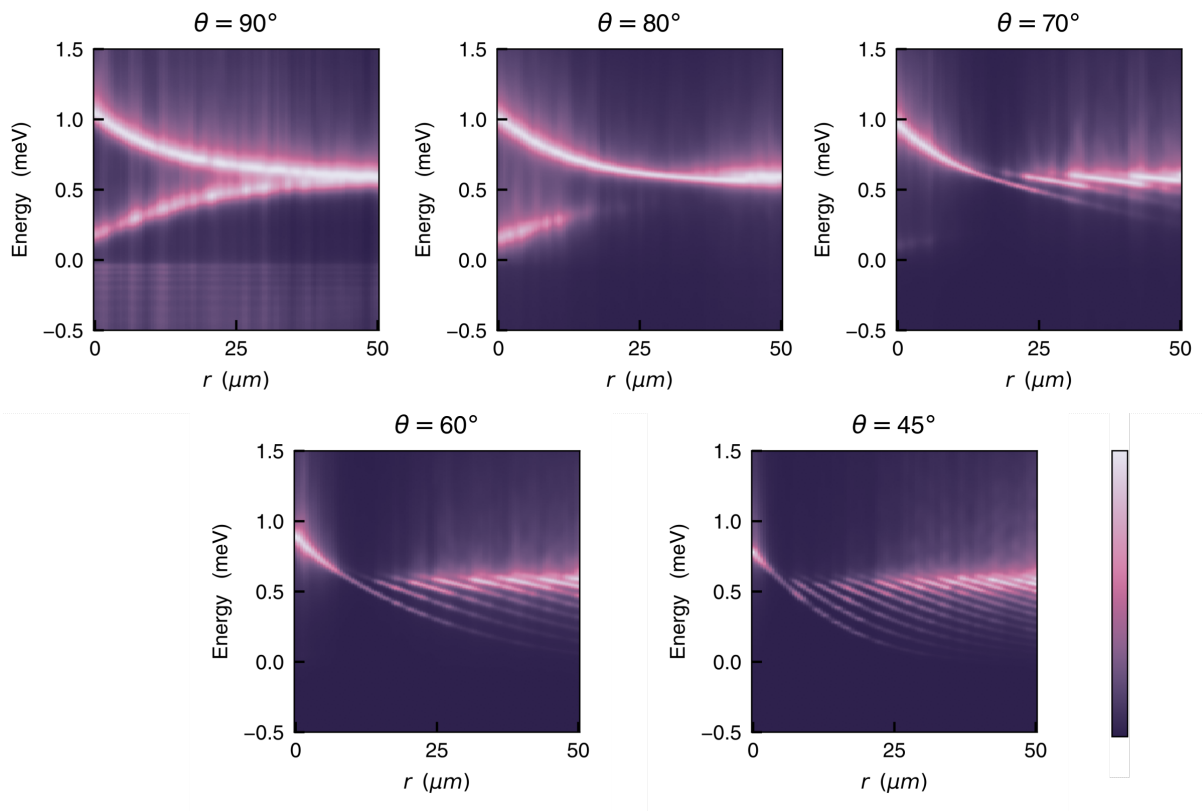


FIG. S2. Calculated dimer spectra as function of the inter-condensate distances for different  $\theta$  reproducing the results depicted in Fig. 3 of the main manuscript.

#### V. CALCULATING PHASE OF THE DIMER

Figure S3 shows the steady-state solution of a condensate driven by two pump spots located at  $\mathbf{r}_{1,2} = \pm r\hat{\mathbf{x}}/2$ , separated by a given distance  $r = |\mathbf{r}_1 - \mathbf{r}_2| = 38 \mu\text{m}$ . Multiple interference fringes can be observed stemming from the propagating polariton waves between the phase locked condensates. These results are similar to the ballistic polariton dimer investigated in [5, 6]. As mentioned above, Eq. (S5) describes the condensate order parameter in the near field. In order to match the obtained numerical results with experiment one needs to Fourier transform the near field wavefunction into an appropriate form which describes the

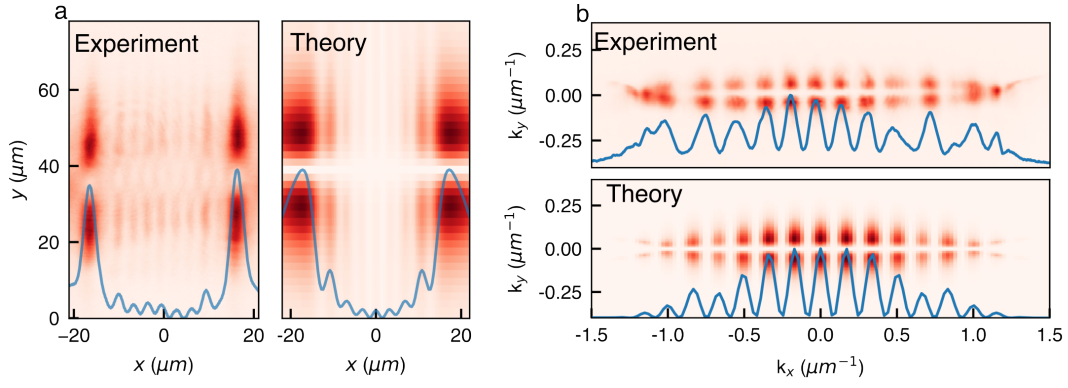


FIG. S3. **a.** PL from an in-phase dimer separated by  $38 \mu\text{m}$  showing 7 fringes in the inter-condensate area, experiment left, theory right. **b.** PL in reciprocal space. There is no PL coming from  $k_y = 0$  for  $|k_y| < 2 \mu\text{m}^{-1}$  or so since the BiC is dark; top experiment, bottom theory. **c.** The number of fringes integrated along  $k_y$  is 14 in accordance with **a.**

measured far field [4],

$$\mathcal{F}^{-1}[k_y \tilde{\psi}(\mathbf{k})] \propto \psi_{\text{FF}}(\mathbf{r}), \quad (\text{S7})$$

where  $\mathcal{F}[\psi] = \tilde{\psi}(\mathbf{k})$ . Figure S3 shows the experimental and simulated dimer condensate density in the far field in both coordinate space and momentum space, side-by-side with excellent agreement. Here, the two condensates form an in-phase (even symmetric standing wave) with an odd number (7) of fringes between them. The real space images of two ballistically coupled condensates shows the two main intensity peaks that originate from the condensates themselves and multiple interference peaks that originate from the phase locking of the two condensates due to polariton flow between them. The two condensates can either be in phase with an odd number of peaks between them, or out of phase with an even number of peaks between the two.

In the analysis presented in Fig. 4 in the main manuscript where we extract the number of fringes, we first integrate the counts of the real space image along the  $y$  axis in order to form a one dimensional data-array along  $x$ . We then proceed by extracting the peaks of the array which correspond to the interference fringes, ignoring the two maximal edge peaks which correspond to the two bright condensate centres. Varying the distance along  $x$  alternates the peaks between odd and even numbers signifying switching between in-phase and anti-phase locking.

## VI. CONFINED MODES IN THE GAP

Figure S4 shows typical spectra of two coupled condensates at different angular orientations. The energy resolved measurements are conducted in such a way that the position at the middle of the distance between the two condensates is aligned on top of the spectrometer's slit. Such measurements were used to extract the mode splitting originating from the evanescent coupling of the two condensates. As illustrated, in some cases the spectrum consists of only two modes, which are taken to be the bonding and anti-bonding mode of the formed polariton molecule. On the other hand, there are cases where the spectrum is consisted of multiple “trapped” modes which originate from the trapping potential induced between the two formed condensates. In our analysis, for extracting the mode splitting due to the evanescent coupling, we always considered the energy difference between the lowest and highest energy state observed in the spectrum. The spectra represented in Fig. 3 in the main text are the result of spatial integration datasets similar to Fig. S4. The blueshift of the data shown in Fig. 3g in the main text has been renormalized to the power recorded during acquisition.

## VII. COUPLING MECHANISM BETWEEN BIC CONDENSATES

We develop a simplified model describing the coupling between the two BiC condensates as a function of angle  $\theta$  with respect to the  $x$ -axis and distance between the pump spots  $r = |\mathbf{r}_1 - \mathbf{r}_2|$  (see Fig. 1f in main text). We assume an ansatz that involves factorization of the condensate wavefunctions as follows,

$$\psi_n(\mathbf{r}) = \sqrt{N_n} X(x - x_n) Y(y - y_n), \quad (\text{S8})$$

where

$$\int |\psi_n(\mathbf{r})|^2 d\mathbf{r} = N_n, \quad (\text{S9})$$

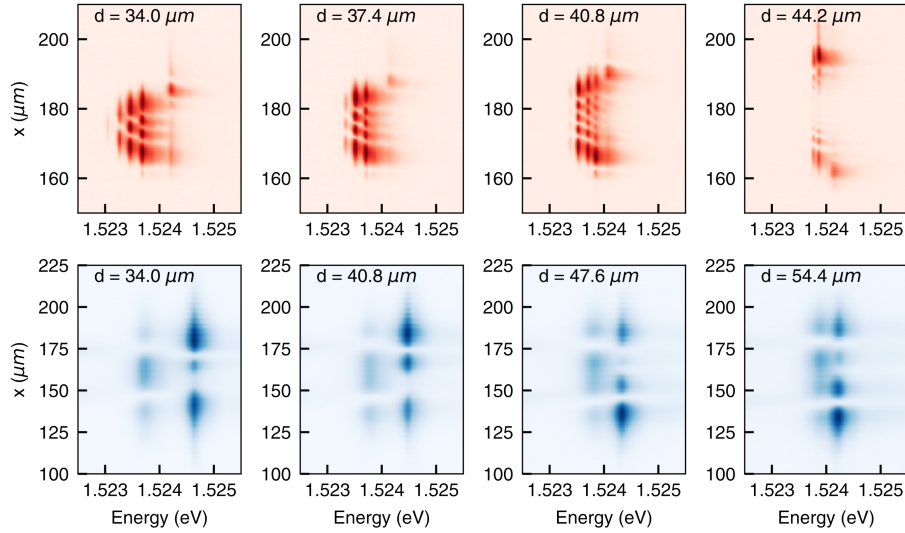


FIG. S4. Typical energy-resolved, coordinate-space PL for a condensate dimer in the ballistic configuration (top row) and on the evanescent one (bottom row). As the dimer separation decreases a trapping potential is formed between two ballistic condensates which gives rise to trapped states in the inter-condensate region. For evanescently coupled condensates decreasing their separation increases the energy splitting of the two molecular states that are formed.

denotes the number of particles in the condensate. A Gaussian profile well describes the wavefunction along the evanescent  $y$ -direction

$$Y(y - y_n) = \frac{1}{\sqrt{\sigma_y} \sqrt{2\pi}} e^{-(y-y_n)^2/4\sigma_y^2}, \quad (\text{S10})$$

where  $\sigma_y$  is a parameter found from fitting to the solutions of Eq. (S5). Along the ballistic  $x$ -direction we have a freely expanding condensate with a rapidly oscillating phase front which we assume to have simple plane wave structure sufficiently far away from the pump spot,

$$X(x - x_n) = \sqrt{\kappa} e^{i(k_c + i\kappa)|x - x_n|}, \quad x \gg w \quad (\text{S11})$$

where  $w$  describes the width of the pump spot in Eq. (S6) and the corresponding condensate bright centre,  $k_c$  is the wavenumber of the condensate outgoing waves and  $\kappa \sim \gamma_{k_c} m_x / 2\hbar k_c$  is the dampening of the profile due to polariton losses  $\gamma_{k_c}$ . We will dismiss the anisotropy of the condensate's density profile for simplicity. This only leads to additional angle-dependent modification of the dimer's coupling strength which will be addressed in later work with more complete description of the condensate profile. For now, we only focus on the relative contribution coming from evanescent and propagating waves towards the dimer's coupling strength.

Determining the coupling strength exactly by solving the corresponding ‘‘hopping energy integral’’ which depends on how much the condensates overlap over their complex-valued potential energy landscape (i.e., pumped regions) and kinetic operator is a challenging task due to the sizes of the condensates and the pumps are comparable to the wavelength of the propagating modes  $w \sim \lambda_c = 2\pi/k_c$ . Instead of relying on numerics, we will adopt the approach in tight-binding theory by defining an ‘‘average hopping energy’’ which is proportional to the overlap between the wavefunctions,

$$J(d, \theta) \propto \int \psi_1^* \psi_2 d\mathbf{r} = e^{-\kappa r \cos(\theta)} \cos[k_c r \cos(\theta)] \cdot e^{-r^2 \sin^2(\theta)/8\sigma_y^2}, \quad (\text{S12})$$

By replacement of  $r_x = r \cos(\theta)$  and  $r_y = r \sin(\theta) = \sqrt{r^2 - r_x^2}$  we obtain Eq. (4) in the main text. The double cosine term controls the sign of the coupling and is responsible for ‘‘in-phase’’ and ‘‘anti-phase’’ locking between the condensates as discussed in detail in Ref. [5, 6]. In agreement with results shown in Fig. 2d,e and Fig. 4c in the main text, as the projected distance  $r_x$ , is varied, the sign of the coupling flips at regular intervals corresponding to a change in the number of interference fringes.

---

\* These two authors contributed equally.

† [dimitrios.trypogeorgos@nanotec.cnr.it](mailto:dimitrios.trypogeorgos@nanotec.cnr.it)

- [1] V. Ardizzone, F. Riminucci, S. Zanotti, A. Gianfrate, M. Efthymiou-Tsironi, D. G. Suárez-Forero, F. Todisco, M. De Giorgi, D. Trypogeorgos, G. Gigli, K. Baldwin, L. Pfeiffer, D. Ballarini, H. S. Nguyen, D. Gerace, and D. Sanvitto, *Nature* **605**, 447 (2022).
- [2] A. Gianfrate, H. Sigurdsson, V. Ardizzone, H. C. Nguyen, F. Riminucci, M. Efthymiou-Tsironi, K. W. Baldwin, L. N. Pfeiffer, D. Trypogeorgos, M. De Giorgi, D. Ballarini, H. S. Nguyen, and D. Sanvitto, *Nature Physics* **20**, 61 (2024).
- [3] F. Riminucci, A. Gianfrate, D. Nigro, V. Ardizzone, S. Dhuey, L. Francaviglia, K. Baldwin, L. N. Pfeiffer, D. Ballarini, D. Trypogeorgos, A. Schwartzberg, D. Gerace, and D. Sanvitto, *Physical Review Letters* **131**, 246901 (2023).
- [4] H. Sigurdsson, H. C. Nguyen, and H. S. Nguyen, *Nanophotonics* **13**, 3503 (2024).
- [5] H. Ohadi, R. L. Gregory, T. Freearde, Y. G. Rubo, A. V. Kavokin, N. G. Berloff, and P. G. Lagoudakis, *Phys. Rev. X* **6**, 031032 (2016).
- [6] J. D. Töpfer, H. Sigurdsson, L. Pickup, and P. G. Lagoudakis, *Communications Physics* **3**, 2 (2020).

---

\* These two authors contributed equally.

† [dimitrios.trypogeorgos@nanotec.cnr.it](mailto:dimitrios.trypogeorgos@nanotec.cnr.it)